Optical Materials 159 (2025) 116622

Contents lists available at ScienceDirect

Optical Materials

journal homepage: www.elsevier.com/locate/optmat

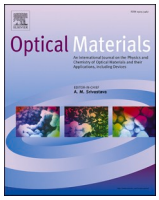

# Interlayer Silicon-Chalcogenide waveguide coupler for heterogeneous integration photonics

Kangjian Bao [a,b,c,1], Boshu Sun [b,c,1], Kunhao Lei [d,1], Yingchun Wu [b,c], Zongxi Li [b,c], Renjie Tang [b,c], Chunlei Sun [b,c], Wei Zhang [e], Hongtao Lin [d], Lan Li [b,c,f,*]

[a] Zhejiang University, Hangzhou, Zhejiang, 310027, China
[b] Zhejiang Key Laboratory of 3D Micro/Nano Fabrication and Characterization, School of Engineering, Westlake University, Hangzhou, 310030, China
[c] Institute of Advanced Technology, Westlake Institute for Advanced Study, Hangzhou, Zhejiang, 310024, China
[d] State Key Laboratory of Modern Optical Instrumentation, Key Laboratory of Micro-Nano Electronics and Smart System of Zhejiang Province, College of Information Science and Electronic Engineering, Zhejiang University, Hangzhou, 310027, China
[e] Zhejiang Key Laboratory of Advanced Optical Functional Materials and Devices, Faculty of Electrical Engineering and Computer Science, Ningbo University, Ningbo, 315211, China
[f] Westlake Institute for Optoelectronics, Fuyang, Hangzhou, 311421, China

ARTICLE INFO

*Keywords:*
Chalcogenide glass photonic devices
Multilayer photonics
Interlayer coupler
$Ge_{28}Sb_{12}Se_{60}$
Subwavelength grating
Polarization rotator

ABSTRACT

Silicon is widely used as the primary material in integrated photonics due to its excellent properties such as low transmission loss, excellent optical confinement, and compatibility with CMOS processes. However, its low nonlinear coefficient and susceptibility to two-photon absorption and free carrier absorption can degrade signal quality and reduce the efficacy of nonlinear interactions, limiting its applications in nonlinear photonics. In contrast, chalcogenide glass, with its superior material nonlinearity and low-temperature deposition process, enables heterogeneous integration that enhances the functionalities of the silicon photonic platform while effectively addressing the limitations of silicon in nonlinear applications. Thus, an interlayer silicon-chalcogenide coupler is essential. In this study, we design three types of interlayer silicon-chalcogenide glass (Si-ChG) couplers: an adiabatic taper coupler, a subwavelength grating coupler, and a polarization rotator coupler, achieving high coupling efficiencies of 99.7 %, 98.5 %, and 98.1 %, respectively, within a compact coupling area size of 30 × 2 μm. Experimentally, a high coupling efficiency of 98.4 % was obtained for the first type of coupler. These interlayer couplers have the potential to further advance Si-ChG heterogeneous integration and nonlinear integrated photonics.

## 1. Introduction

Rapid data transmission and computational demands growth necessitate versatile, high-performance, and cost-effective integrated photonic architectures. In recent years, densely integrated, multilevel photonic integrated circuits (PICs) have developed rapidly due to their innovative capabilities and superior energy efficiency. Silicon, with its potential for low-cost manufacturing and established compatibility with complementary metal-oxide-semiconductor (CMOS) technology, has demonstrated the capability to generate, manipulate, and detect optical signals on ultra-compact chips. This characteristic makes silicon an ideal candidate for integrating photonic functions onto micro-scale devices, leveraging the extensive infrastructure and manufacturing economies of scale inherent in the CMOS industry. Consequently, silicon photonics holds the promise of revolutionizing various sectors by enabling smaller, faster, and more energy-efficient photonic components for applications ranging from data communication to sensing and computing. However, inherent limitations in silicon fundamentally constrain its performance in many application scenarios. With a bandgap of 1.1 eV, silicon is prone to two-photon absorption (TPA) in the near-infrared region. The intensity-dependent absorption coefficient restricts its application in high-power scenarios, such as parametric amplification [1,2], Raman

This article is part of a special issue entitled: 80th birthday of Giancarlo C. Righini published in Optical Materials.

* Corresponding author. Zhejiang Key Laboratory of 3D Micro/Nano Fabrication and Characterization, School of Engineering, Westlake University, Hangzhou, 310030, China.
*E-mail address:* lilan@westlake.edu.cn (L. Li).

[1] Contributed equally to this work.

https://doi.org/10.1016/j.optmat.2024.116622
Received 23 October 2024; Received in revised form 23 December 2024; Accepted 28 December 2024
Available online 8 January 2025

lasing [3,4], and Brillouin amplification [5–8]. The plasma effect caused by free carriers generated through TPA results in photon absorption, leading to energy loss and unwanted heat generation. Both TPA and free-carrier absorption are significant challenges in high-performance silicon photonics. To overcome these drawbacks and improve device performance on silicon platforms, materials with superior nonlinear properties have been integrated with silicon through innovative structural designs, creating a new heterogeneously integrated platform. This platform not only mitigates the limitations of silicon but also expands device functionality based on the properties of the heterogeneous materials, meeting the requirements for on-chip photonic devices that exhibit low-loss, low-power consumption, high efficiency, low noise, nonlinear parametric processes, and large spectral transparency windows suitable for high-speed optical information processing, optical interconnects, and optical computing.

Currently, various materials, including silicon nitride ($Si_3N_4$) [9–11], silicon carbide (SiC) [12–14], lithium niobate ($LiNbO_3$) [15–17], and chalcogenide glasses (ChGs) [18–20], have been developed to address the limitations of silicon. Table 1 provides a comparative analysis of the photonic properties of Si, $Si_3N_4$, SiC, $LiNbO_3$, and ChGs. Among these, chalcogenide glasses are particularly notable for their high material nonlinearity, low two-photon absorption, strong light confinement in photonic waveguides, and tunable dispersion characteristics. Additionally, the capability to fabricate chalcogenide glass waveguides at low temperatures allows for monolithic integration on various substrates, making them particularly attractive for the development of high-speed and nonlinear photonic devices.

To achieve effective monolithic integration of Silicon and ChG, a high-efficiency interlayer coupler is essential. Using $Ge_{28}Sb_{12}Se_{60}$, (GeSbSe), a commonly used ChG material, this study presents three Si-GeSbSe interlayer coupler designs demonstrating high coupling efficiencies for Si-ChG interlayer coupling. Each design achieves a simulated coupling efficiency exceeding 98 % within a compact area of 30 μm × 2 μm. We experimentally demonstrated an interlayer coupler based on an adiabatic taper with a coupling efficiency of 98.4 % (@1550 nm), meeting the coupling loss requirements for nonlinear optics on a chalcogenide platform.

## 2. Device design and fabrication

We designed and optimized the structure of the Si-GeSbSe interlayer waveguide couplers using 3D Finite Difference Time Domain (FDTD) simulations, including couplers based on an adiabatic taper, sub-wavelength grating (SWG), and a polarization rotator. During the experimental demonstration, we encountered significant fabrication constraints. For instance, the SWG segments were always partially missing during the fabrication of the SWG, and the alignment tolerance of the rib waveguide on the polarization rotator was extremely demanding. Therefore, we experimentally implemented the interlayer coupler based on the adiabatic taper and are still optimizing our fabrication process to try to fabricate the SWG coupler and the polarization rotator coupler.

### 2.1. Interlayer coupler based on adiabatic taper

As shown in Fig. 1a–b, the coupler is designed using two adiabatic tapers of length $L_{taper}$. To minimize transmission loss, the width of the incident single-mode silicon waveguide $W_{in}$ is 0.5 μm, and the waveguide height $H_{in}$ is 0.22 μm. Meanwhile, the emerging GeSbSe waveguide uses a waveguide with a width $W_{out}$ of 0.84 μm and a height $H_{out}$ of 0.3 μm. To meet the phase-matching condition and reduce reflections caused by the abrupt refractive index change at the taper tip, the width of the taper waveguide should be minimized. However, due to fabrication limitations, the silicon taper tip width $W_1$ and the GSSe taper tip width $W_2$ are both uniformly set to 150 nm in this study.

The phase-matching condition can be expressed as:

$$n_{eff1} = n_{eff2}, \tag{1}$$

where $n_{eff1}$ is the effective refractive index of the tapered silicon waveguide, and $n_{eff2}$ is the effective refractive index of the tapered GeSbSe waveguide.

Taking a 150 nm interlayer coupling gap $H_1$ and a 30 μm coupling zone length $L_{taper}$ as an example, Finite Difference Eigenmode (FDE) simulations were utilized to model different widths of the silicon and GeSbSe waveguides. The simulations show that the phase-matching condition is met when the silicon waveguide width narrows to 0.343 μm and the GeSbSe waveguide tapers are set to 0.519 μm (Fig. 1c). The simulated transmission over taper length (also coupling length) and the electric field distribution of the coupler based on this parameter in the xz plane (@1550 nm) are depicted in the following Fig. 1d. The result shows when the taper length exceeds 30 μm, the transmission can be higher than −0.01 dB (99.7 %) and the remaining power is suppressed to below −25 dB. And Fig. 1e illustrates the electric field distribution of the silicon-based chalcogenide interlayer coupler in the xz plane (@1550 nm) when the coupling length is 30 μm.

To fabricate this coupler, we first used a standard silicon-on-insulator (SOI) wafer to create the silicon taper using electron beam lithography (EBL) and inductively coupled plasma (ICP) etching, as shown in Fig. 1f. Following this, $SiO_2$ was deposited via plasma-enhanced chemical vapor deposition (PECVD). To achieve a flat coating surface, chemical-mechanical polishing (CMP) was performed on the deposited $SiO_2$

**Table 1**
Comparison of the optical properties of materials suitable for integration with silicon photonic platforms.

| Material | Si | $Si_3N_4$ | SiC | $LiNbO_3$ | ChG |
|---|---|---|---|---|---|
| Bandgap (eV) | 1.1 | 5 | 3.2 | 4 | NA |
| Transparent window (μm) | 1.1–5.5 | 0.3–4.6 | 0.2–2 | 0.35–5.5 | 0.6–25 |
| Refractive index | 3.5 | 1.98 | 2.6 | 2.2 | 2.0–3.5 |
| TNC $n_2$( × $10^{-7}$ $cm^2$/GW | 450 (@1.5 μm) | 24(@1.5 μm) | 80(@1.5 μm) | 18(@1.06 μm) | 290-900(@1.5 μm) |
| TPA coefficient $\alpha_2$ (@1.55 μm) (cm/GW) | 0.79 | Negligible | Negligible | 16.5 | 0.01 |
| FOM ($=\frac{n_2}{\alpha_2\lambda}$) | 0.37 | ≫1 | ≫1 | 0.43 | 18.7–58 |
| Typical Optical Loss (dB/cm) | ~1 | ~0.01 | ~0.1 | ~0.027 | ~0.5 |
| Heterogeneous integration process | – | Monolithic integration (high-temperature film preparation process) | Hybrid integration (Complex wafer bonding processes) | Hybrid integration (Complex wafer bonding processes) | Monolithic integration (low-temperature film preparation process) |
| Reference | [3,5–8] | [9] | [12] | [15] | [18] |

TNC: Three-order nonlinear coefficient; FOM: Figure of Merit.

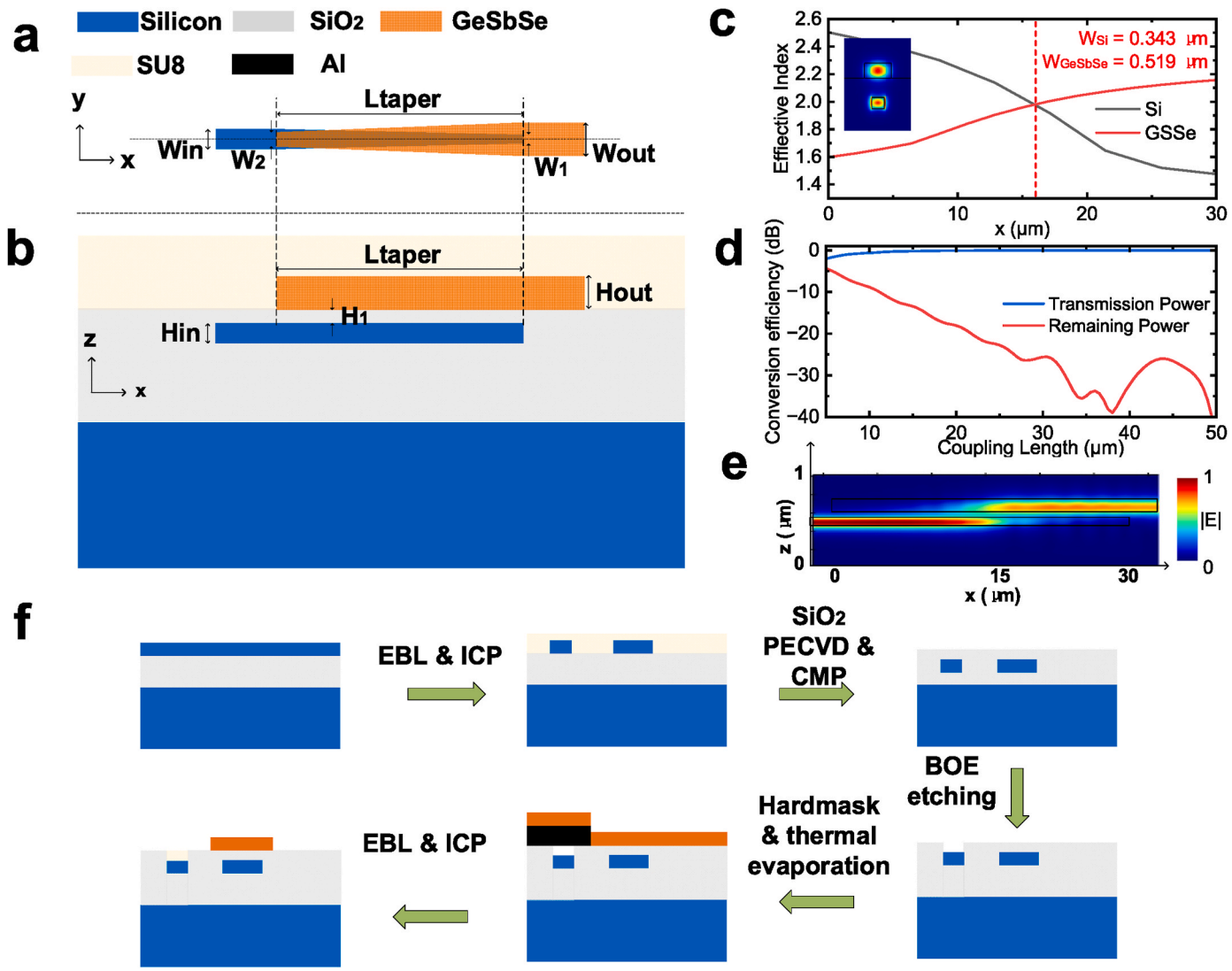


**Fig. 1.** Simulation and experiment data for interlayer coupler based on adiabatic taper. (a) Top view of interlayer coupler based on adiabatic taper; (b) Side view of interlayer coupler based on adiabatic taper; (c) Effective refractive index and mode field of the interlayer adiabatic coupler's tapered waveguide along the x-direction (@1550 nm); (d) Simulated transmission power (from Si to GSSe waveguide) and remaining power of the interlayer coupler under different coupling lengths; (e) Electric field distribution of the silicon-based chalcogenide interlayer coupler in the xz plane (@1550 nm); (f) Fabrication processes of the interlayer coupler based on adiabatic taper. (For interpretation of the references to color in this figure legend, the reader is referred to the Web version of this article.)

layer. Next, buffered oxide etching (BOE) was used to open a window for the alignment markers, and an Al hard mask was applied to avoid the window being filled during the GeSbSe deposition. Subsequently, a 300 nm GeSbSe layer was deposited using thermal evaporation, followed by another round of EBL and ICP etching to fabricate the upper GeSbSe taper.

### 2.2. *Large-alignment-tolerance interlayer coupler based on sub-wavelength grating (SWG) waveguide*

Due to the stringent alignment requirements for the dual-layer structure and the narrow silicon waveguide width in adiabatic couplers, conventional adiabatic couplers often fail to achieve their ideal coupling efficiency in practical fabrication. To maintain high coupling efficiency despite overlay errors, interlayer couplers with high overlay tolerance are required. Subwavelength grating (SWG) waveguides, with their flexible structures and low-loss transmission properties, are frequently used to modulate refractive index dispersion, polarization, and other properties.

We employed a low-loss SWG waveguide structure to expand the mode field area significantly, thereby increasing the overlay tolerance of the interlayer couplers. The SWG-based interlayer coupler is illustrated in Fig. 2a–b. The taper waveguides are replaced with SWG waveguides with varying widths, and fishbone-type grating waveguides with lengths $L_1$ and $L_2$ for the Silicon and GeSbSe waveguides, respectively, are used as a transition between the single-mode and SWG waveguides to mitigate losses and reflections due to abrupt refractive index changes. The $L_1$ and $L_2$ are both set as 10 μm.

Low-loss transmission in SWG waveguides is contingent upon certain conditions that only Bloch waves with wavelengths much larger than the Bragg wavelength can undergo low-loss transmission, given by:

$$\lambda \gg 2n_{eff}{}^{*}\Lambda, \tag{2}$$

where $\lambda$ is the wavelength of light, $n_{eff}$ is the effective refractive index of the SWG waveguide and $\Lambda$ is the period of the SWG.

The FDTD method was used to simulate the periodic SWG structure. A SWG waveguide with a period of 0.3 μm and a duty cycle of 0.5 for both silicon and GSSe waveguides meet the requirements for low-loss transmission and interlayer coupling. According to the dispersion curve in Fig. 2c, when the lower silicon-based SWG waveguide width $W_4$

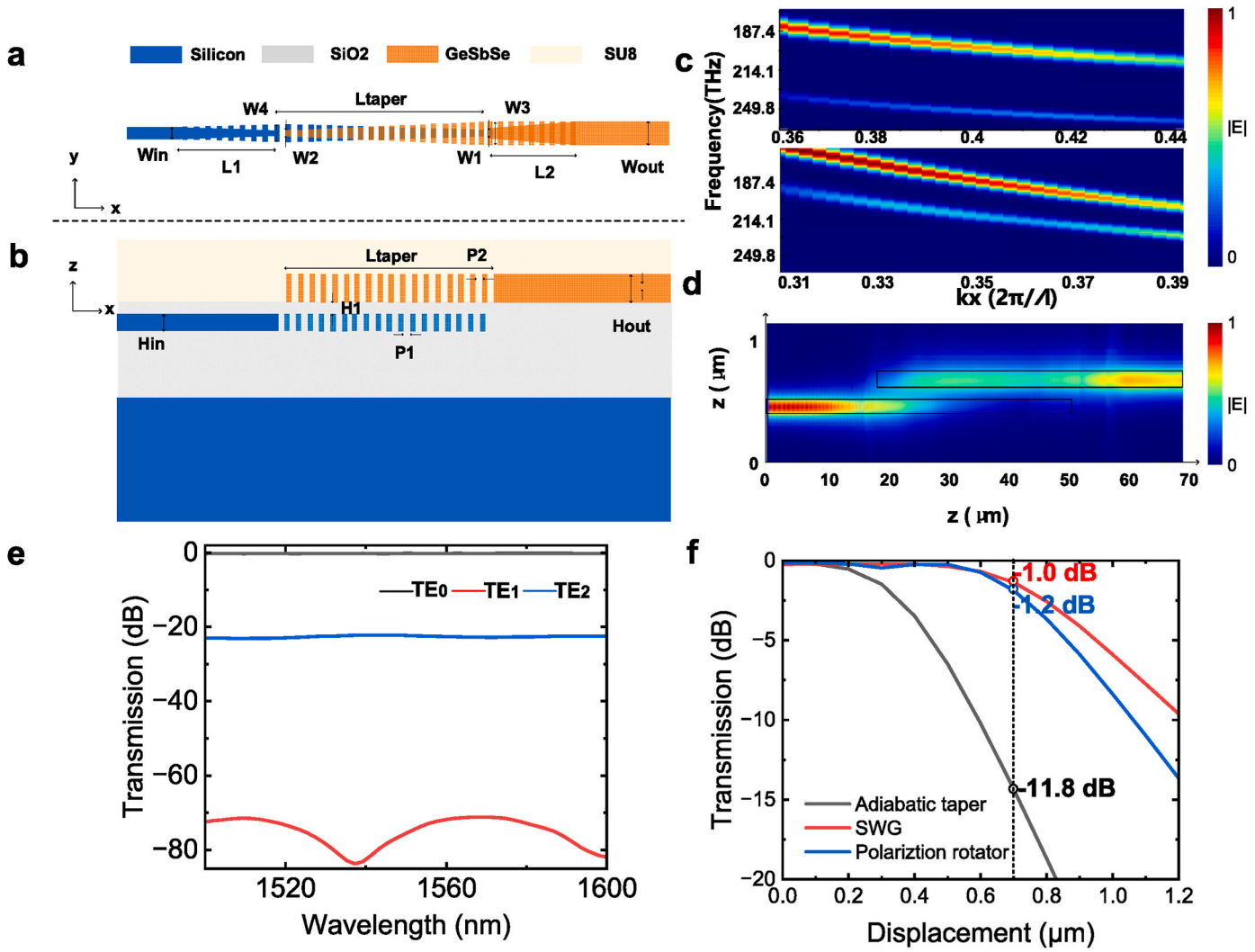


**Fig. 2.** Interlayer coupler based on SWG. (a) Top view of interlayer coupler based on SWG; (b) Side view of interlayer coupler based on SWG; (c) Dispersion curve of periodic SWG waveguides (upper: 0.8-μm-width Si waveguide, lower: 2-μm-width GeSbSe waveguide, kx is the wave vector); (d) Electric field distribution in xz plane of Si-GeSbSe interlayer coupler based on SWG (insets are Different waveguide electric field distributions for Si waveguides (left: conventional waveguide, right: SWG waveguide)); (e) Simulated coupling high-order-mode crosstalk of Si-GeSbSe interlayer coupler based on SWG; (f) Simulated coupling efficiency of SWG interlayer coupler, adiabatic taper and polarization rotator interlayer coupler under different process deviations (y direction displacement).

is 0.8 μm, the effective refractive index is approximately 1.963, and the wavelength is much larger than the corresponding Bragg wavelength (1063 nm), enabling low-loss transmission. Similarly, the effective refractive index of the upper GeSbSe SWG waveguide with a width $W_3$ of 2 μm is approximately 1.896, with the wavelength significantly larger than its corresponding Bragg wavelength (1168 nm), also allowing for low-loss transmission. The linear taper SWG coupler based on these structural parameters satisfies the phase-matching conditions required for conventional adiabatic couplers, achieving efficient interlayer coupling. The electric field distribution of the SWG-based coupler in the xz plane is shown in Fig. 2d. The coupling efficiency and mode crosstalk performance of this interlayer coupling were also simulated, as shown in Fig. 2e. The suppression of higher-order modes is lower than −22 dB.

Due to the refractive index modulation enabled by the SWG waveguide, the effective refractive index of the silicon taper waveguide is significantly reduced, increasing the fabrication tolerance and maintaining high coupling efficiency even with larger overlay errors. As illustrated in Fig. 2f, compared to conventional interlayer couplers, the SWG coupler retains a coupling efficiency of −1.0 dB (79.4 %) under an overlay error of approximately 0.7 μm, far surpassing the −11.8 dB (6.6 %) coupling efficiency of adiabatic couplers. This structure mitigates efficiency reduction due to fabrication-induced errors, demonstrating process insensitivity and contributing to the development of efficient silicon-chalcogenide platforms.

### 2.3. Interlayer coupler based on polarization rotator

To address the challenge of increasing layer spacing and minimizing inter-layer crosstalk in multi-layer photonic integrated circuits, we propose a dual-layer adiabatic coupler based on a polarization rotator. By employing transverse magnetic (*TM*) polarization for coupling, inter-layer crosstalk can be effectively reduced without increasing the coupling length. *TM* polarization exhibits stronger coupling strength due to its longer evanescent field in the waveguide's vertical direction compared to transverse electric (*TE*) polarization. Fig. 3a–c illustrate the schematic of the dual-layer adiabatic coupler based on a polarization rotator, divided into five sections. The waveguides of the polarization rotator are designed as rib waveguides. The rib waveguide height of Si, $H_{rib1}$, and GSSe, $H_{rib2}$, are both 150 nm. The Si slab waveguide height, $H_{slab1}$, and the GSSe slab waveguide height, $H_{slab2}$, are 70 nm and 150 nm, respectively. In region i-ii, light initially enters from a single-mode waveguide in the lower silicon layer and transits from the $TE_0$ mode to

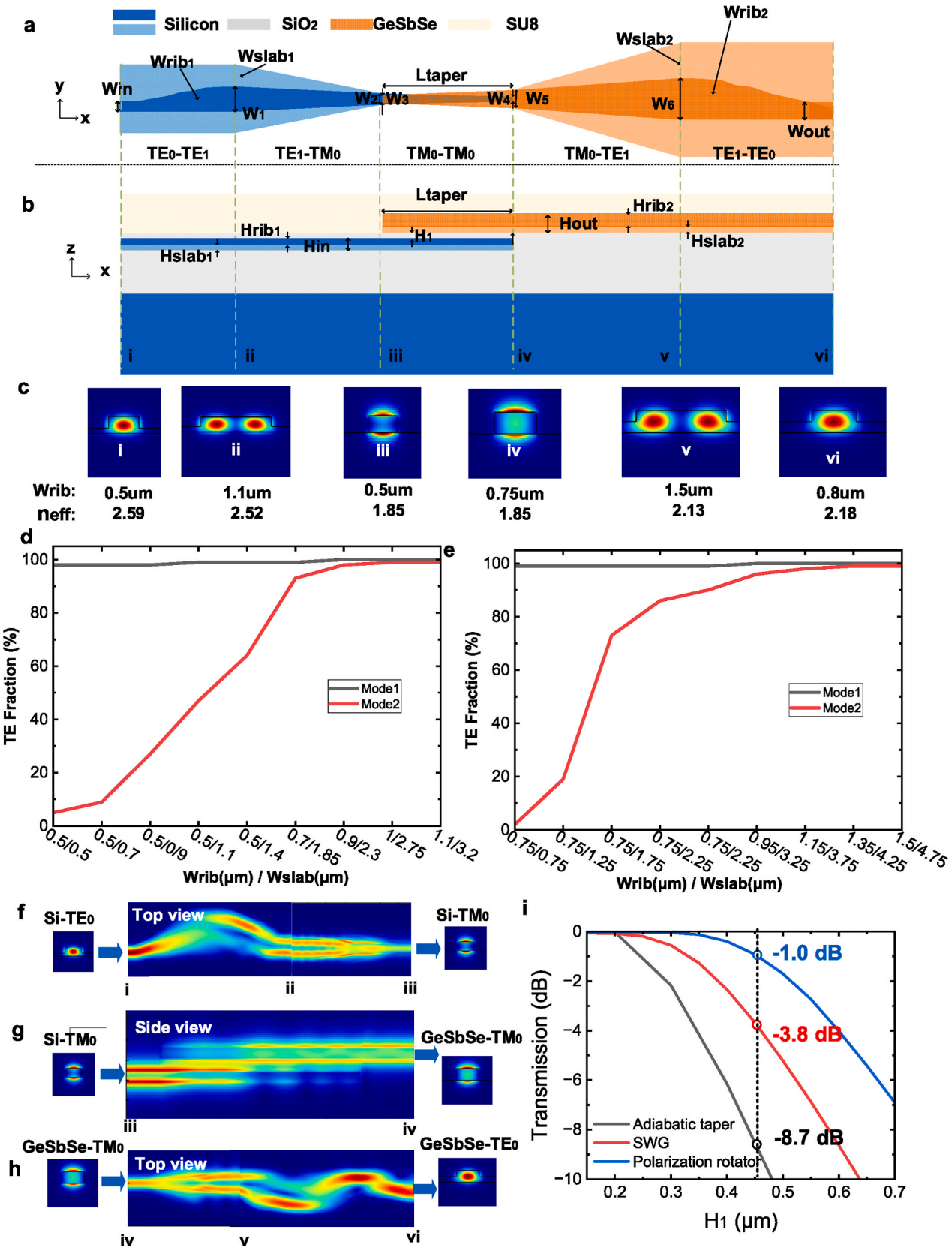


**Fig. 3.** Interlayer coupler based on polarization rotator. (a) Top view of interlayer coupler based on polarization rotator; (b) Side view of interlayer coupler based on polarization rotator; (c) Mode profiles at the corresponding area of the waveguides; (d) and (e) *TE* polarization component ratio with waveguide width changes of Si and GeSbSe, respectively; (f)–(h) Electric field distribution of interlayer coupler polarization rotator over xz plane for (f)Si–Si *TE-TM* interlayer coupler (g) Si-GeSbSe *TM-TM* interlayer coupler (h) GeSbSe-GeSbSe *TM-TE* interlayer coupler; (i) Coupling efficiency of interlayer coupler based on adiabatic taper, SWG and polarization rotator under different $H_1$. (The light colors denote slab waveguide and the dark colors are rib waveguide in (a) and (b).). (For interpretation of the references to color in this figure legend, the reader is referred to the Web version of this article.)

the higher-order $TE_1$ mode through a rib waveguide with a gradient width optimized using the particle swarm optimization algorithm, forming a $TE_0 - TE_1$ mode converter [21,22]. Subsequently, the conversion from the $TE_1$ mode to the $TM_0$ mode is achieved by adjusting the width of the rib waveguide and the slab layer in region ii-iii. In this part, the widths of the rib and slab Si waveguides are adjusted as inversely shown in Fig. 3d. Each interval of the positions in Fig. 3d is 3 μm. In regions iii-iv, the Si waveguide changes gradiently from 500 nm to 150 nm width, with an inverse gradient width from 150 nm to 750 nm for the GSSe waveguide, enabling the $TM_0$ mode in the Si waveguide to transfer to the $TM_0$ mode in the GSSe waveguide. Next, the conversion from the $TM_0$ mode to the $TE_1$ mode is achieved by adjusting the width of the rib waveguide and the slab layer in regions iv-v, as shown in Fig. 3e. Each interval of the positions in Fig. 3e is 4 μm. Finally, we applied a $TE_1$ -$TE_0$ mode converter in the GSSe waveguide again using the particle swarm optimization algorithm [21,22].

This mode conversion is realized by calculating the *TE* polarization fraction across different positions in the waveguide. A mode with a 100 % *TE* polarization fraction signifies pure *TE* polarization, while a mode with 0 % *TE* polarization fraction indicates pure *TM* polarization. A hybrid mode has a *TE* polarization fraction between 0 % and 100 %, with higher values close to 50 % indicating significant mode mixing. When inputting $TM_0$ and $TE_0$ modes, the *TE* polarization fraction of the waveguide mode is calculated as shown in Fig. 3d–e.

Fig. 3f–h present the mode field transmission distribution of the polarization rotator. The results show that the input $TE_0$ mode in the Si waveguide is initially converted to the $TM_0$ mode (from regions i to iii). Subsequently, the $TM_0$ mode in the Si waveguide is transferred to the $TM_0$ mode in the GeSbSe waveguide (from regions iii to iv), and finally, the $TM_0$ mode in the GeSbSe waveguide is converted to the $TE_0$ mode in the output GeSbSe waveguide (from regions iv to vi). At 1550 nm, the conversion efficiency from $TE_0$ to $TM_0$ reaches 98 % (from regions ii to iii). With a dual-layer spacing of 150 nm at 1550 nm, the coupling efficiency of the TM adiabatic coupler exceeds 98.5 %, and the coupler dimensions are 30 μm × 0.75 μm. Additionally, as shown in Fig. 3i, the inter-layer coupling efficiency of the polarization rotator-based coupler remains above −1.0 dB (79.4 %) even with a 0.46 μm thick isolation layer. This is significantly higher than the −3.8 dB (41.7 %) efficiency of the SWG coupler and the −8.7 dB (13.5 %) efficiency of the adiabatic taper coupler at the same isolation layer thickness.

## 3. Results and discussion

To characterize the coupling efficiency performance of the Si-ChG interlayer coupler, a tunable laser (TSL 550, Santec) was employed, as shown in Fig. 4a. Given the low loss of the coupler, it is challenging to effectively characterize it using a single device. Therefore, we cascaded multiple interlayer couplers to measure their cumulative loss. Fig. 4b displays the insertion loss between 1545 nm and 1555 nm. To reduce the influence of the Fabry-Perot effect, we smoothed the curves by connecting the averages of the wave crests and troughs. We linearly fit the insertion loss of the interlayer coupler at 1550 nm, as shown in Fig. 4c. The results indicate a coupling loss of −0.070 ± 0.013 dB per coupler (98.4 % coupling efficiency) at 1550 nm, demonstrating efficient interlayer coupling in a silicon-chalcogenide heterogeneous integration platform.

Table 2 summarizes the performance of the three interlayer couplers designed in this study. All the couplers achieved simulated coupling efficiencies above 95 % and the experimental coupling efficiency of the first-type coupler is over 95 %. Each coupler type has its unique advantages: the adiabatic taper coupler is characterized by low fabrication complexity, the SWG coupler exhibits high fabrication tolerance over the xy plane, and the polarization rotator coupler demonstrates the highest coupling efficiency with high fabrication tolerance over z direction among the three designs.

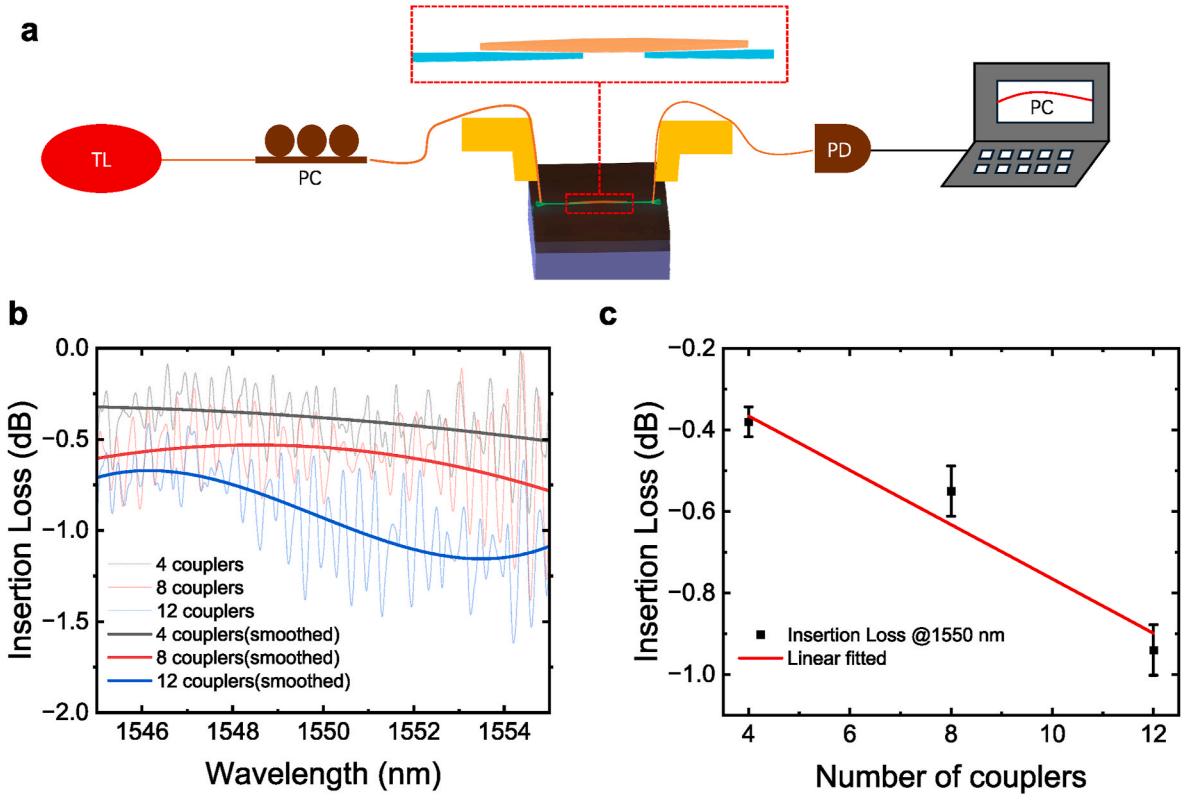


**Fig. 4.** Characteristic system and experiment data. (a) Characterization system (TL: Tunable laser, PC: Polarization controller, PD: Photodetector, PC: Personal Computer); (b) Measured Insertion loss of the interlayer coupler based on adiabatic taper (gc: grating coupler); (c) Linear fitted insertion loss of the interlayer coupler (@1550 nm).

**Table 2**
Performance comparation of interlayer couplers.

| Structure | Material | Fabrication Processes | Coupling efficiency (%) | Size (μm) | Reference |
|---|---|---|---|---|---|
| Grating Coupler | Si - SiN | LPCVD (800 °C) | 64(s) | 100 × 20 | [23] |
| Evanescent coupler | Si - SiN | LPCVD (775 °C) | 88.9(e) | 300 × 4 | [24] |
| Metastructure-based interlayer directional coupler | Si - SiN | PECVD (400 °C) | 24(e) | 20 × 4 | [25] |
| SiNx-Si metamaterial coupler | Si - SiN | PECVD (400 °C) | 87(e) | 10 × 5 | [26] |
| Edge coupler | SiN – SiO2 | PECVD (400 °C) | 82(e) | / | [27] |
| Adiabatic taper coupler | a-Si:H - AlN | PECVD (400 °C) | ~94.6(s) | 40 × 1 | [28] |
| Adiabatic taper coupler | SiN - SiN | LPCVD (800 °C) | 70.8(e) | 350 × 0.74 | [29] |
| Slope waveguide coupler | a-Si:H - a-Si:H | PECVD (400 °C) | 91.2(s); 89.7(e) | 8.24 × 1.44 | [30] |
| Adiabatic taper coupler | Si -GeSbSe | ThE(30 °C) | 99.7(s) 98.4 (@1550 nm)(e) | 30 × 0.84 | This work |
| SWG coupler | Si - GeSbSe | ThE(30 °C) | 98.5(s) | 30 × 2 | This work |
| Polarization rotator coupler | Si - GeSbSe | ThE(30 °C) | 98.1(s) | 30 × 0.75 | This work |

s: simulation; e: experiment; ThE: Thermal Evaporation; LPCVD: Low Pressure Chemical Vapor Deposition.

## 4. Conclusions

This study aimed to design and optimize Si-GeSbSe interlayer couplers for photonic integrated circuits using FDTD and FDE numerical simulations. The research systematically investigated the impact of waveguide shape and size, interlayer distance, coupling offset, and wavelength on coupling efficiency and crosstalk. By employing a linearly tapered waveguide structure, the study demonstrated efficient coupling over short lengths by mitigating refractive index mismatches and optimizing the waveguide width transition. The design resulted in an ultra-compact interlayer coupler measuring less than 30 μm × 2 μm. Experimentally, a coupling efficiency of 98.4 % was achieved. Additionally, the study optimized the process on a heterogeneously integrated platform by refining the CMP parameters of the intermediate layer to mitigate adverse effects from multi-layer processes on second-layer device performance. To address higher optical power coupling requirements, two high-efficiency interlayer coupler designs were also simulated and proposed: a SWG coupler with high misalignment tolerance and a high-efficiency coupler based on a polarization rotator. Each design achieved interlayer coupling efficiencies above 98 % by simulation (@1550 nm).

In conclusion, this research deepens the theoretical understanding of silicon-chalcogenide interlayer coupler design and demonstrates its practical relevance in heterogeneous integration photonic devices by achieving high coupling efficiencies and optimizing device performance, advancing the field of nonlinear photonics and integrated photonic device technology.

## CRediT authorship contribution statement

**Kangjian Bao:** Writing – review & editing, Writing – original draft, Visualization, Validation, Software, Investigation, Data curation. **Boshu Sun:** Methodology, Investigation, Data curation. **Kunhao Lei:** Visualization, Methodology, Investigation. **Yingchun Wu:** Writing – review & editing, Methodology. **Zongxi Li:** Writing – review & editing. **Renjie Tang:** Writing – review & editing. **Chunlei Sun:** Writing – review & editing, Visualization, Supervision. **Wei Zhang:** Investigation. **Hongtao Lin:** Supervision. **Lan Li:** Writing – review & editing, Supervision, Investigation, Funding acquisition, Conceptualization.

## Declaration of competing interest

The authors declare that they have no known competing financial interests or personal relationships that could have appeared to influence the work reported in this paper.

## Acknowledgments

The authors acknowledge the support from Zhejiang Provincial Natural Science Foundation of China (Grant No. LD22F040002), Special Support Plan for Photoelectric Chips Research at Westlake University [Grant No. 10300000H062401/001] and the Key Project of Westlake Institute for Optoelectronics [Grant No. 110500Y0022303]. The authors would like to acknowledge Westlake Center for Micro/Nano Fabrication and Instrumentation, and ZJU Micro-Nano Fabrication Center at Zhejiang University for their facility support. Furthermore, the authors extend their gratitude to Xinyu Qiao for his help in GSSe film deposition.

## Data availability

The relevant data supporting the conclusions of this study can be obtained from the corresponding author, contingent upon a reasonable request.

## References

[1] X. Liu, R.M. Osgood, Y.A. Vlasov, W.M.J. Green, Nat. Photonics 4 (2010) 557–560.
[2] D. Heydari, M. Catuneanu, E. Ng, D.J. Gray Jr., R. Hamerly, J. Mishra, M. Jankowski, M.M. Fejer, K. Jamshidi, H. Mabuchi, Optica 10 (2023) 430–437.
[3] H. Rong, A. Liu, R. Jones, O. Cohen, D. Hak, R. Nicolaescu, A. Fang, M. Paniccia, Nature 433 (2005) 292–294.
[4] H. Rong, S. Xu, O. Cohen, O. Raday, M. Lee, V. Sih, M. Paniccia, Nat. Photonics 2 (2008) 170–174.
[5] H. Shin, W.J. Qiu, R. Jarecki, J.A. Cox, R.H. Olsson, A. Starbuck, Z. Wang, P. T. Rakich, Nat. Commun. 4 (2013) 1–10.
[6] T.K. Liang, H.K. Tsang, Appl. Phys. Lett. 85 (2004) 3343–3345.
[7] W.J. Qiu, P.T. Rakich, H. Shin, H. Dong, M. Soljacic, Z. Wang, Opt Express 21 (2013) 31402–31419.
[8] E.A. Kittlaus, N.T. Otterstrom, P.T. Rakich, Nat. Commun. 8 (2017) 15819.
[9] J. Liu, G. Huang, R.N. Wang, J. He, A.S. Raja, T. Liu, N.J. Engelsen, T. J. Kippenberg, Nat. Commun. 12 (2021) 2236.
[10] D.J. Moss, R. Morandotti, A.L. Gaeta, M. Lipson, Nat. Photonics 7 (2013) 597–607.
[11] D.T.H. Tan, K.J.A. Ooi, D.K.T. Ng, Photon. Res. 6 (2018) B50–B66.
[12] S. Wang, M. Zhan, G. Wang, H. Xuan, W. Zhang, C. Liu, C. Xu, Y. Liu, Z. Wei, X. Chen, Laser Photon. Rev. 7 (2013) 831–838.
[13] P. Xing, D. Ma, K.J.A. Ooi, J.W. Choi, A.M. Agarwal, D. Tan, ACS Photonics 6 (2019) 1162–1167.
[14] I.V. Kityk, M. Makowska-Janusik, A. Kassiba, K.J. Plucinski, Opt. Mater. 13 (2000) 449–453.
[15] J.T. Lin, F. Bo, Y. Cheng, J.J. Xu, Photon. Res. 8 (2020) 1910–1936.
[16] C. Wang, M. Zhang, M. Yu, R. Zhu, H. Hu, M. Loncar, Nat. Commun. 10 (2019) 978.
[17] R. Cheng, M. Yu, A. Shams-Ansari, Y. Hu, C. Reimer, M. Zhang, M. Lončar, Nat. Commun. 15 (2024) 3921.
[18] S. Serna, H.T. Lin, C. Alonso-Ramos, A. Yadav, X. Le Roux, K. Richardson, E. Cassan, N. Dubreuil, J.J. Hu, L. Vivien, Photon. Res. 6 (2018) B37–B42.
[19] D. Xia, Y.F. Huang, B. Zhang, P.Y. Zeng, J.X. Zhao, Z.L. Yang, S.W. Sun, L.Y. Luo, G. Y. Hu, D. Liu, Z.F. Wang, Y.F. Li, H.R. Guo, Z.H. Li, Laser Photon. Rev. 16 (2022) 2100443.
[20] D. Xia, Z.L. Yang, P.Y. Zeng, B. Zhang, J.Y. Wu, Z.F. Wang, J.X. Zhao, J.T. Huang, L. Y. Luo, D. Liu, S.X. Yang, H.R. Guo, Z.H. Li, Laser Photon. Rev. 17 (2023) 2200219.
[21] D.G. Chen, X. Xiao, L. Wang, W. Liu, Q. Yang, S.H. Yu, Opt Lett. 41 (2016) 1070–1073.
[22] H. Guan, Y. Ma, R. Shi, A. Novack, J. Tao, Q. Fang, A.E.-J. Lim, G.-Q. Lo, T. Baehr-Jones, M. Hochberg, Opt. Lett. 39 (2014) 4703–4706.

[23] M. Sodagar, R. Pourabolghasem, A.A. Eftekhar, A. Adibi, Opt. Express 22 (2014) 16767–16777.
[24] N. MacFarlane, M.R. Kossey, J.R. Stroud, M.A. Foster, A.C. Foster, Apl Photonics 4 (2019).
[25] Y.S. Yang, H. Zhao, X.M. Ren, Y.Q. Huang, Opt Express 29 (2021) 28912–28923.
[26] P. Xu, Y. Zhang, S. Zhang, Y. Chen, S. Yu, Opt. Lett. 44 (2019) 1230–1233.
[27] Y.X. Liang, Z.H. Li, S.J. Fan, J. Feng, D.P. Liu, H.J. Liao, Z.H. Yang, J.B. Feng, N. D. Cui, Opt Lett. 47 (2022) 4786–4789.
[28] S. Zhu, G.-Q. Lo, J. Lightwave Technol. 34 (2016) 386–392.
[29] M. Girardi, O.B. Helgason, A. Caut, M. Karlsson, A. Larsson, V. Torres-Company, Opt Express 31 (2023) 31435–31446.
[30] R. Petra, S.Z. Oo, A. Tarazona, R. Cernansky, S.A. Reynolds, A.Z. Khokhar, V. Mittal, D.J. Thomson, A. Politi, G.Z. Mashanovich, G.T. Reed, H.M.H. Chong, Opt Express 27 (2019) 15735–15749.